Electronic properties of Pb islands on graphene: Consequences of a weak interface coupling from a combined STM and *ab initio* study

V. Cherkez, P. Mallet, T. Le Quang, L. Magaud, and J.-Y. Veuillen

Univ. Grenoble Alpes, CNRS, Institut Néel, 38000 Grenoble, France

By means of scanning tunneling microscopy and spectroscopy, we investigate the electronic properties of lead islands (width 5–100 nm, thickness 5–25 monolayers) deposited by molecular beam epitaxy on twisted graphene layers grown on SiC(000-1). We find that elastic scattering processes govern the local density of states probed at the surface of the Pb islands, inducing (i) the well-known quantum well states due to electron confinement in the direction perpendicular to the surface and (ii) spatial in-plane periodic modulations related to quasiparticle interferences off the island edges. Through a quantitative analysis of these effects, compared with *ab initio* calculations for a two-dimensional Pb slab, we conclude that the lead islands grown on the surface of graphene can be considered as freestanding from the point of view of their electronic structure, leaving the surrounding graphene layer unperturbed. Accordingly, low bias tunneling spectra show evidence of a sizable interface resistance. Nevertheless, we suggest that the transparency of the interface, which can be estimated from its resistance, is good enough to induce superconductivity within the underlying graphene layer by proximity effect with the Pb islands.

I. INTRODUCTION

Physical properties of atomically thin crystalline lead films have attracted considerable interest in the past. They can be easily grown with precise atomic thickness on a wide range of metallic and semiconducting substrates, making them a convenient model system for the systematic study of the thickness-dependent properties of metallic films. For example, thickness modulation of their electrical resistivity [1,2], Hall coefficient [3,4], work function [5,6], surface energy, and thermal stability [6–10] have been observed and related to the quantum size effect. Lead is also a particularly interesting example of a conventional superconductor with a relatively high critical temperature ($T_C = 7.19$ K in bulk [11]). This makes it attractive for the experimental study of the superconductivity in low-dimensional systems. Thus, the evolution of the critical temperature, superconducting gap, and electron-phonon coupling were studied down to the ultimate two-dimensional (2D) limit of the few-atomic layers [12–20]. The dependence of these physical quantities on the film thickness and their microscopic origin are an active subject of research; they are tentatively attributed to the combined effects of the reduced dimensionality and interface with the substrate (see Ref. [21] for a review). Moreover, flattop islands (incomplete films) allow further confinement of superconductivity to 0D [22–24], whereas the interface between the islands and supporting substrate is accessible for the spatially resolved study of the superconducting proximity effect thoroughly investigated for the case of Pb/Si(111) system [25–28]. Finally, confinement effects have been studied in pyramidal Pb nanocrystals weakly coupled to an InAs substrate [29] by scanning tunneling microscopy (STM) and spectroscopy (STS), resolving the energy and wave functions of the discrete electronic states in different regimes of quantum confinement.

This system allowed to experimentally address the Anderson limit for superconductivity in 0D systems [30].

In a first approximation, a thin metallic film can be modeled as a quantum well due to the electron confinement in the direction perpendicular to the surface [31]. The resulting electronic structure consists of 2D bands related to quantum well states (QWS). These bands can be derived from the bulk band structure of the parent material tuned by the quantization of the electron wave vector in the direction of the confining potential. The energies of onset of the QWS in the center of the Brillouin zone can be understood from the so-called phase accumulation model [31–33], while their full 2D dispersion can usually be found with density functional theory (DFT) calculations.

In practice, metallic films are always prepared on a surface of a supporting material, which inevitably influences their atomic and electronic structure. In general, the QWSs preserve their intrinsic character only within the substrate bulk band gap (full or partial). The overlap with the substrate bands leads to a strong quasiparticle scattering and decreases their lifetime in the film [34,35]. Moreover, the QWS dispersion can be significantly modified by interaction with a substrate and new bands can appear [36–41]. As a result, the film with the substrate must be considered as a combined system. For example, in the case of Pb films on Si(111) the angle-resolved photoemission spectroscopy (ARPES) [42,43] and STM/STS [44–46] measurements revealed a complete flattening of the QWS bands close to the center of the Brillouin zone as compared to the calculated nearly free electron dispersion in a freestanding film.

To reduce the film-substrate interaction and to explore the limit of freestanding metallic films it was suggested to use graphite or graphene as substrates for the metal deposition

[47–51]. These materials are chemically inert at the surface and they have a large partial gap in their band structure. The ARPES measurements [49,50] have indeed revealed the strong resemblance between freestanding lead films and lead films grown on graphitic layers or highly oriented pyrolitic graphite (HOPG).

The Pb/graphene system presents another particular interest since graphene may acquire superconducting properties in proximity with superconducting lead. Graphene-superconductor devices demonstrate many unique properties [52–57] which are related to the particular band structure of graphene, the high mobility of charge carriers, and the ease to tune their density. While a considerable progress in the transport studies of such devices was done in recent years, a thorough local-scale investigation of the proximity effect at the graphene-superconductor interface is still challenging [58,59].

In the present paper, we analyze the electronic structure of Pb islands with well-defined heights grown on twisted graphene multilayers using low-temperature STM and STS. We first establish that their electronic states close to the Fermi level (both in occupied and empty states) behave essentially as for freestanding Pb layers since (i) the line shapes and widths of the QWS related structures, (ii) the in-plane band dispersion, and (iii) the lifetime of the quasiparticles are almost identical to the theoretical predictions. These findings confirm previous results from ARPES studies [49,50] (performed on an ensemble of islands with different heights), extending their conclusions to low-lying empty states and to a larger range of island thicknesses. Therefore, the electronic properties of thin Pb films supported on graphene, including superconductivity, should be close to those of unsupported layers. Additionally, our measurements show that the lead islands do not perturb the electronic states of graphene in their vicinity, as revealed by the absence of both charge doping and electron scattering. Together with the limited stability of the metal islands under the STM tip, these observations point again to a weak bonding between the substrate and the lead film, consistent with the quasi-freestanding character of the latter. We observe a size-dependent dip at zero bias in the density of state (DOS) of the Pb islands by STS. In line with the weak coupling of the electronic states at the metal-substrate interface and following previous works [60], we ascribe this dip to a sizable resistance (of the order of the quantum of resistance) at the Pb-graphene junction. Finally, we discuss the possible existence of the superconducting proximity effect in graphene below the lead islands. We estimate that the transparency of the graphene/Pb interface is moderate (the electron tunneling rate across the interface is of the order of bulk Pb superconducting gap), which, according to the previously published theoretical analysis [61–64], is sufficient to induce a measurable superconducting gap in graphene. Thus we suggest that this system is a good candidate for further low-temperature STM study of the proximity induced superconductivity in graphene.

II. METHODS

Twisted graphene layers [65] were grown on the surface of 6H-SiC(000-1) (C face) following the procedure described in Ref. [66]. After the growth, the sample was transferred into a separate ultrahigh vacuum (UHV) setup and outgazed. The surface of the sample consisted of 100–500-nm-wide single-crystal domains with a characteristic moiré pattern [65] inside domains (period of moiré 1–15 nm). The clean-surface graphene layer had a very low electron doping [67] ($<3\times10^{11}$ cm^{-2}) as deduced from the quasiparticle interference (QPI) pattern measurements [68,69] and from the position of the Van Hove singularities associated with the moiré pattern [70,71]. Lead was deposited *in situ* with a homebuilt evaporator, at the rate 0.2 ML/min on the surface kept at room temperature.

Most of the presented results were obtained with a home-built low temperature STM operating at 8.5 K [except image of Fig. 1(a) obtained at 40 K with another UHV setup]. At such temperature, the islands are not superconducting. In all cases, we use mechanically sharpened PtIr tip (postannealed in UHV), and the data were collected with a bias applied to the sample. Depending on the sample bias and tip condition, the apparent heights of the Pb islands measured by STM can change by as much as 0.14 nm (i.e., 0.5 ML). Such effect was recently reported for thin lead islands grown on Si(111)6×6-Au surface [72]. It was ascribed to the unequal spilling of different QWS wave functions into the vacuum. In the present paper, the thickness of the islands in monolayer (ML) units was obtained by dividing their apparent height as measured by STM by the Pb $\langle 111 \rangle$ interlayer distance (0.286 nm [73]) and by rounding to the integer value. For the spectroscopic measurements, the differential conductance dI/dV was measured with the standard lock-in technique (amplitude of the bias modulation 4–12 mV, frequency 477 Hz). In the energy range [−2.5 eV; +2.5 eV], the open feedback loop mode (constant height or Z_{const}) was used. At higher positive bias >+2.5 eV the closed feedback loop mode (constant current or I_{const}) was used. Data analysis was performed with WSxM software [74]. All energies are given relative to the Fermi level E_F.

DFT calculations were performed using the VASP code with the projector-augmented wave approach [75,76]. The slab consists of a $1\times1\times28$ cell that contains 14 layers of lead stacked in face centered cubic (fcc) configuration and separated by an equivalent empty space (3.76 nm), which is large enough to avoid spurious interaction through the vacuum. The PBE exchange and correlation is used [77]. Integration in the Brillouin zone is performed using the tetrahedron method on a grid $21\times21\times4$. After convergence, residual forces on the atoms are smaller than 0.01 eV·Å^{-1}. The experimental Pb fcc lattice parameter (a = 3.50 Å [73]) was used within the planes and relaxation along z direction was allowed except for atoms in the middle of the slab that were kept fixed. We have checked that calculation with a = 3.56 Å, the optimized bulk Pb lattice parameter, does not have a significant quantitative influence on the onsets and dispersion of the QWSs in the energy range from −2.5 eV to +2.5 eV.

III. RESULTS AND DISCUSSION

We first characterize the morphology of Pb islands grown on the surface of multilayer graphene. Figure 1(a) shows a typical STM image of the surface after the deposition of few MLs of lead. The growth proceeds by the Volmer-Weber
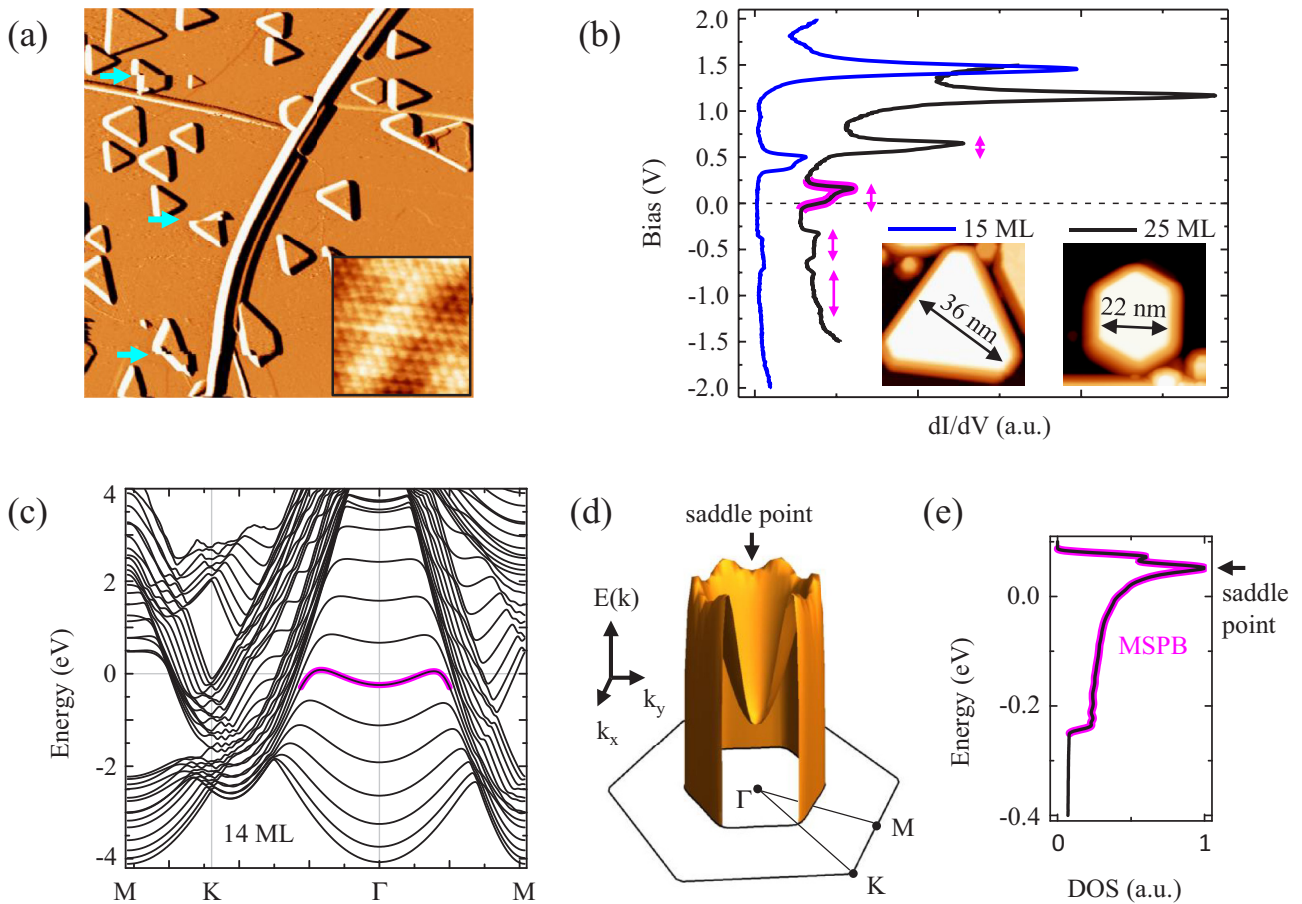
FIG. 1. (a) Derivative (dz/dx) of a constant current STM image (image size, 1000×1000 nm^2; sample bias, -500 mV; tunnel current, 50 pA; $T = 40$ K), showing Pb islands grown on the surface of multilayer graphene on SiC(000-1). Nominal Pb coverage is 4 ML. Light-blue arrows point to the Pb islands occasionally moved by the STM tip during scanning. Inset: Atomic resolution on a lead island (4×4 nm^2; 12 mV; 400 pA; $T = 8.5$ K). (b) dI/dV(V) spectra measured at $T = 8.5$ K in the center of two Pb islands of different thickness (shown in the inset). For the spectrum measured on top of the 25-ML-thick island, one of the rectangular-shape peaks is highlighted with magenta, the width of the peaks is indicated with magenta arrows. For the spectrum measured on the 15 ML island, the set point parameters were sample bias, 2 V; tunnel current, 300 pA. For the 25-ML-thick island, the dI/dV curve is combined from two spectra: one taken in the bias range [1.5 V; -1.0 V] with the set point 1.5 V; 300 pA; another one taken in the bias range [0.25 V; -1.5 V] with the set point 0.25 V; 100 pA; the amplitude of the two spectra were properly rescaled. (c) Calculated band structure of a freestanding 14-ML Pb(111) film. The energy is measured in eV relative to the Fermi level. For one of the bands, its M-shaped part (MSPB) near the Brillouin zone center is highlighted with magenta. (d) 3D representation E(k_x, k_y) of the highlighted MSPB from (c). (e) Calculated DOS corresponding to the band from (d).

mode. As one can see, most of the islands have the shape of truncated triangles. Atomic lattices on their tops [inset of Fig. 1(a)] have triangular symmetry with the periodicity of 3.52 Å (the interatomic distance of bulk Pb in the (111) plane is 3.50 Å [73]). The close-packed rows run parallel to the edges of the island. These facts suggest that the islands have fcc crystal structure with one of the ⟨111⟩ axes oriented perpendicular to the surface (the hexagonal close packed (hcp) crystal structure would result in a hexagonal shape of the islands [78]). This is the commonly observed atomic structure for thin lead films [78]. The width and the height of the islands vary in the range of 5–100 nm and of 5–25 ML, respectively.

The islands are weakly attached to the surface. STM measurements performed at room temperature revealed only a clean graphene surface, presumably because all islands were swept by the STM tip. Cooling the surface down to 40 K significantly improves the stability of the islands, while

the tip still occasionally moves them during the scan [e.g., islands shown with the light-blue arrows in Fig. 1(a)]. Similar observations of the tip-island interaction were reported previously [51,79,80].

We have studied the possible influence of the deposited lead islands on the electronic structure of the surface graphene layer. In particular, we have checked the possible change in the doping of the graphene at the contact with lead. The doping level of twisted bilayer graphene can be conveniently estimated by STS from the position of the Van Hove singularities relative to the Fermi level [70,71]. According to our results [67], lead deposition does not produce any significant doping of the surface graphene layer at the distances larger than few nanometers from the islands edge (it is impossible to perform STS measurements closer to the islands due to the finite radius of curvature of the tip). Moreover, STM images [67] show the absence of intervalley quasiparticle scattering
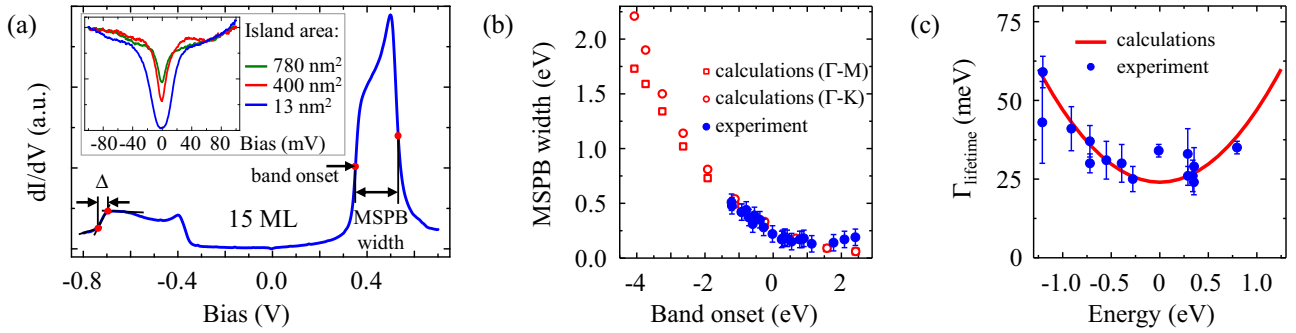
FIG. 2. (a) dI/dV spectrum measured at $T = 8.5$ K in the center of the 15-ML island from Fig. 1(b). Red dots on the rectangular-shaped peak on the right indicate the band onset and the MSPB width. The procedure used to extract the lifetime broadening $\Gamma_{lifetime}$ is shown on the left peak, two red dots highlight the intersection points from which the width of the band onset Δ is evaluated. Inset: Pseudogap measured at $T_{sample} = 8.5$ K in the vicinity of the Fermi level on three islands with different area (spectra normalized at -100 mV, linear background subtracted). (b) The width of the MSPB versus band onset. The experimentally measured values are extracted from the dI/dV curves obtained in Z_{const} mode. The theoretical values are extracted from our DFT calculations. (c) The quasiparticles lifetime broadening $\Gamma_{lifetime}$ versus energy. The experimentally measured values are extracted from the width of the band onsets in the Z_{const} mode (see text for details). The calculations take into account the electron-electron and electron-phonon interactions (see text for details).

(i.e., the absence of the $(\sqrt{3} \times \sqrt{3})R30°$ pattern [68,69]) on the graphene regions nearby the edges and corners of Pb islands. This indicates the absence of abrupt potential change [81] or strong chemical bonding [82] at the island boundary. We also did not observe [67] evidence of intravalley quasiparticle scattering close to Pb islands in graphene domains with Bernal stacking [68,69,83]. We conclude that graphene's electronic structure remains intact under lead islands, with vanishing backscattering of bare graphene electrons at the island boundaries.

These observations already point to the weak coupling between the lead islands and the graphene.

To get further evidence of the weak interaction between these materials, we will concentrate in the following on the electronic structure of the deposited Pb islands. For sufficiently large islands (with size >15 nm), it is dominated by the electron confinement in the direction perpendicular to the surface and is equivalent to the electronic structure of atomically thin metallic films [35,46]. In Fig. 1(b), the STS spectra recorded in the center of 15-ML and 25-ML islands (as deduced from the apparent height measured by STM) are shown. At biases below +0.5 V, they consist of a series of peaks of a rectangular shape [one of them is highlighted with magenta color in Fig. 1(b)]. We compare these spectra with the DFT-calculated band structure. For example, we show in Fig. 1(c) such a calculation for a 14-ML thick (14 atomic planes) freestanding lead film in the fcc stacking. We have verified that it is in a good agreement with the previously reported results of similar simulations [2,6,84,85].

We attribute the rectangular-shaped peaks in the spectra to the M-shaped parts of the bands (MSPB) near the center of the Brillouin zone [one of them is highlighted with magenta color in Fig. 1(c)]. The MSPB corresponds to the states with small in-plane wave vector and hence should give the main contribution to the dI/dV signal [86]. A 3D representation of the computed MSPB crossing the Fermi level [the one marked with magenta in Fig. 1(c)] is shown in Fig. 1(d). One notes the free-electron-like dispersion of the band near the center of the 2D Brillouin zone. At larger k-vectors, it

changes to a steep and anisotropic downward dispersion. In between, at the turning region, a complex wavy E(k) surface is formed. Its maximum appears at slightly higher energy in the ΓK direction than in the ΓM direction, but this difference gradually vanishes for the QWS at higher energies. The DOS corresponding to this part of the QWS is shown in Fig. 1(e). As one can see, the main features in the DOS come from the MSPB. They closely resemble the shape of the rectangular peaks in the spectra shown in Fig. 1(b) and in the more detailed spectrum shown in Fig. 2(a). The steplike onset of the peaks in the spectra [Figs. 1(b) and 2(a)] and in the computed DOS [Fig. 1(e)] both correspond to the onset of the QWS at Γ. The two peaks in the DOS around 0.05 eV in Fig. 1(e) are related to the top of the MSPB. The more intense peak originates from the saddle points in the ΓM direction and the weaker peak corresponds to the top of the MSPB in the ΓK direction. The separation between these peaks is too small to be resolved in our experiment and we only observe a pronounced maximum near the top of the MSPB in the spectra. We also observe that the rectangular-shaped peaks become narrower and acquire a Lorentzian shape at higher energy [Fig. 1(b)], in accordance with the flattening of the MSPB in the calculated band structure [Fig. 1(c)]. The flattening entails proportional increase of the DOS which is partially responsible for the increasing intensity of the peaks in the STS spectra. Another effect that contributes to the increase of the spectral intensity is the higher transparency of the tunnel barrier at high positive (relative to the tip) bias. Finally, the separation between the peaks decreases when the thickness of the island is increased [see Fig. 1(b)], which can be intuitively understood within the phase accumulation model [31–33].

We conclude that the experimental spectra are in a qualitative agreement with the calculated band structure of a freestanding lead film. However, previous studies have shown that the substrate has an important effect on the film's electronic structure. The most prominent example is the Pb/Si(111) system, where the MSPB appear to be flattened at all energies [42–44,46,87]. This fact was attributed to a strong interaction between lead and silicon, which probably leads to the

distortion of lead atomic lattice [88]. A rectangular-shaped signature of the MSPB in the spectra was observed for the Pb islands on Ag(111) [35] and Cu(111) [20] surfaces. The partial band gap existing at the surface of these metals protects the QWS in lead film from the coupling with the substrates bulk states. Beyond the gap, the electron confinement in the film is strongly reduced, which translates into a strongly decreased quasiparticle lifetime and in the smearing of the MSPB peaks in the spectra [20,35].

To quantify the degree of coupling between lead islands and graphene and to get more precise information about the electronic structure of the islands, we study in more detail the spectroscopic signatures of the QWS. For example, the spectrum of Fig. 2(a) was measured in the center of the same 15 ML island as the one shown on Fig. 1(b) and it covers a narrower energy range with only two MSPB—one above and one below the Fermi level.

One of the characteristic features of the lead film band structure which is accessible in our experiments is the width of the MSPB. In Fig. 2(b), we plot its values extracted from the STS spectra as a function of the QWS onset energy. The band onset was defined as the midpoint of the rising slope of the rectangular peak in the STS spectrum [Fig. 2(a)]. For the higher energy range ($>+1.5$ eV) where the MSPB becomes narrow [as in Figs. 1(b) and 1(c)], the onset of the QWS was defined as the maximum of the Lorentzian-shape peak. The width of the MSPB was defined as the energy difference between the midpoints of the rising and falling slopes of the peak in the spectrum [Fig. 2(a)]. Comparison with our DFT calculations shows a good agreement for the onset energies $E < +1$ eV, at variance with the case of Pb films on Si(111) mentioned above, once again pointing toward a small lead-graphene coupling. At higher energies, the intrinsic width of the MSPB becomes comparable with the quasiparticle lifetime broadening (see below) and the width of the peaks in spectra is no more directly related to the band structure.

From the experimental spectra, we can also extract the quasiparticle lifetime broadening $\Gamma_{lifetime}$ as a function of energy. To do this, we closely follow the procedure described in Ref. [35]. Namely, in the energy range $<+1$ eV, $\Gamma_{lifetime}$ is related to the width Δ of the rising slope of the rectangular-shaped MSPB peaks in the dI/dV curves through $\Gamma_{lifetime} = (2/\pi)\Delta$ [35]. The geometrical construction used for the extraction of the slopes width Δ is illustrated on the left-hand MSPB of Fig. 2(a).

In the absence of defects, the quasiparticle lifetime broadening is determined by the electron-electron (Γ_{e-e}) and electron-phonon (Γ_{e-ph}) interactions. Residual scattering on the defects (including the interface with the substrate) and instrumental broadening give a total contribution Γ_0. The total lifetime broadening is equal to $\Gamma_{e-e} + \Gamma_{e-ph} + \Gamma_0$. Following the arguments of Refs. [35,46], we assume constant values of the electron-phonon interaction and of the residual broadening Γ_0 in the whole energy range considered. For the contribution from electron-electron interactions we utilize the Quinn-Ferrell expression [89] $\Gamma_{e-e} = \alpha(E - E_F)^2$, with $\alpha = 0.023\,\text{eV}^{-1}$ [35,46]. The total calculated lifetime broadening is plotted in Fig. 2(c) for the constant value of $\Gamma_{e-ph} + \Gamma_0 = 29$ meV taken from Ref. [35].

The experimental values of lifetime broadening are plotted in Fig. 2(c) for the energy range $[-1.25$ eV; 1.25 eV]. We have also analyzed the values of the lifetime broadening at higher energies $[1.25$ eV; 3.5 eV] (not shown here). For the energy range >-0.4 eV (up to 3.5 eV), our experimental observations are in a very good quantitative agreement with the results of the same measurements in the Pb/Ag(111) system [35], indicating similar low defects and interface scattering. The major difference between the measured quasiparticle lifetime broadening in the lead films on graphene and on silver is observed below -0.4 eV. This energy corresponds to the edge of the partial band gap at the surface of Ag(111). Below this energy, Pb QWS at the Brillouin zone center are coupled to the bulk bands of silver, which translates into the divergence of the quasiparticle lifetime broadening. On the contrary, at the surface of graphene the lifetime broadening continues to follow the predictions of the Quinn-Ferrell formula down to -1.2 eV, owing to the extended partial band gap in the reciprocal space of the substrate.

There is another distinct signature of the weak electronic coupling between lead and graphene. The STS spectra on the islands systematically show a pseudogap at the Fermi level [see the inset of Fig. 2(a)]. Its width and depth increase when the area of the island is decreased. Similar observations for the lead islands on the surface of HOPG were reported previously [60], with comparable widths and depths of the pseudogap. As explained by these authors, such observations result from dynamical Coulomb blockade due to a relatively high resistance (of the order of resistance quantum 25.8 kΩ) at the lead/graphite interface. We expect a similar mechanism at the lead/graphene interface. Notice that such effect is absent for the Pb islands on metallic substrates [20,60].

We continue our study by considering the QPI pattern detected at the edges of the lead islands. Recently, similar observations were reported for the few-layer lead films formed above Ar-filled nanocavities on the Pb(111) surface [84,85]. However, the small size of the cavities led to the complete lateral confinement of the QWS. Our experimental observations on a very small island (<10 nm) are in a qualitative agreement with the results of Ref. [85]. Similarly, discrete states of 0D Pb nanocrystals were analyzed in Ref. [29]. Here we will concentrate on the QPI pattern at the edges of the islands with lateral size larger than the coherence length of the quasiparticles.

Figure 3 presents the results of STS measurements along the line passing across the 25-ML island (arrow in the STM image insert on the left). As can be seen on the average spectrum (Fig. 3, on the left), three MSPBs fall into the energy range covered by the measurement. The image on the right gives an explicit representation of the spatial and energy dependence of the dI/dV signal (gray-scale coded) across the island. Vertical profile on this image gives the spectrum at a given point along the line, whereas horizontal profile gives the dI/dV signal across the island at a given bias. It is clear that both edges of the island (corresponding to the left and right sides of the image) induce oscillatory modulation of the local density of states (LDOS). Within each MSPB, the wavelength of the interference pattern strongly depends on the energy: it amounts to approximately 1 nm in the center of MSPB and diverges at its bottom and top. On the contrary, the periodicity
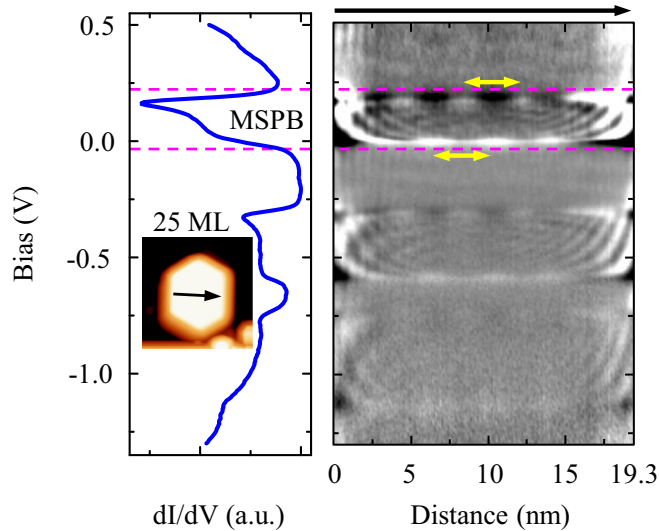
FIG. 3. Results of the spectroscopic measurements along a line on top of the 25-ML island from Fig. 1(b). The spectra were measured in 200 equidistant points along the 19.3-nm line. Left: average spectrum; inset: topographic image of the island with the black arrow indicating the position and direction of the spectroscopic line. Right: dI/dV(x,V) map resulting from these spectroscopic measurements. Bright (dark) color indicates large (small) signal. Yellow arrows indicate the periodic modulation of the intensity at the bottom and top edges of the MSPB due to the moiré pattern in the underlying graphene.

of the QPI pattern is almost energy independent between the MSPB and is about 0.5–0.6 nm.

We also note the long-range modulation of the spectral intensity, indicated with yellow arrows on the figure, at the bottom and top of the MSPB. This long-range modulation has the periodicity of the moiré pattern in the underlying graphene (which appears due to the twist angle between the two topmost

graphene layers [65]). Importantly here, the moiré pattern is not related to the Pb/graphene interface. Moiré patterns arising from the interface have been discussed for Pb islands grown on Si(111), and ascribed to both geometric [90] or electronic [91,92] effects. For this strongly coupled system, the moiré pattern induces local shifts (by tens of meV) of the spectroscopic features [91,92], whereas in the present case, the weak Pb/graphene coupling only induces small (of the order of 5%) modulation of the amplitude of the LDOS at the MSPB edges.

We check on the right image of Fig. 3 that the phase of the LDOS modulations induced by the moiré pattern changes by π across each MSPB. The same effect is seen for one MSPB of a 15-ML thick island in Fig. 4(b) (line spectroscopy) and Fig. 5(a) (2D spectroscopic image). These observations can be interpreted using a phenomenological model, where the influence of the moiré pattern of graphene is described by a weak 2D periodic potential acting on the states of a Pb layer. The electronlike states (with upward band dispersion) at the bottom of the MSPB and the holelike states (with downward band dispersion) at the top of the MSPB then respond to this potential in opposite ways. For instance, the LDOS at a given position is maximum (minimum) for electronlike states close the potential minima, whereas it is minimum (maximum) for holelike states (this can be readily proven in one dimension following a textbook approach [11]).

To get more quantitative information about the origin of the QPI pattern, we show in Fig. 4 the results of a similar spectroscopic measurement along the line going from one of the edges of the 15-ML island toward its center [see the black arrow on the inset on Fig. 4(a)]. Here the energy range covered by each spectrum [the average spectrum is shown in Fig. 4(a)] is narrower, it contains only one MSPB (from -0.74 V to -0.34 V) and a large portion of the band structure between two successive MSPBs (from -0.34 V to $+0.30$ V). In Fig. 4(b), one can see the details of the LDOS modulation as a function of energy and distance from the edge. The
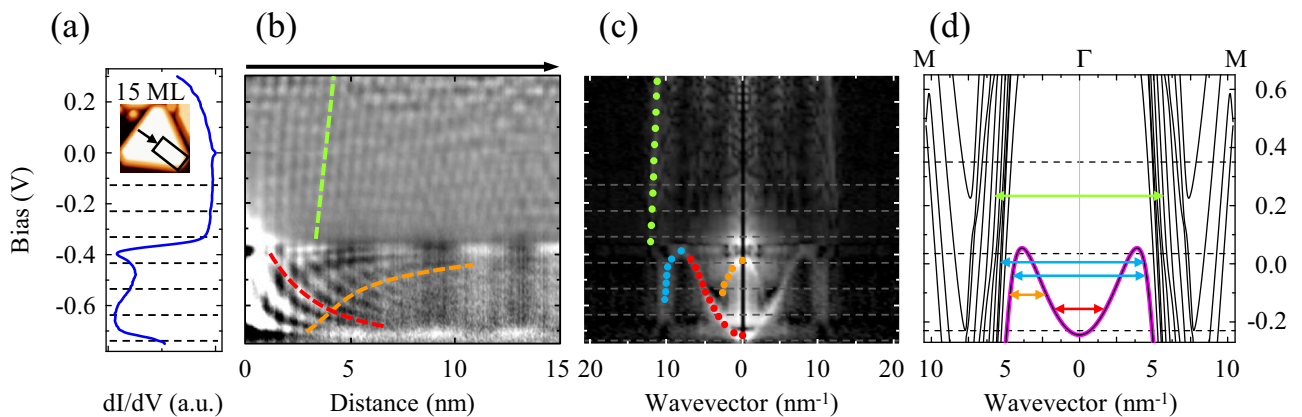

FIG. 4. Results of the spectroscopic measurements along a line on the top of the 15 ML island from Fig. 1(b). (a) Average spectrum; inset: Topographic image of the island with the black arrow indicating the position and direction of the spectroscopic line. Black rectangle shows the place where the constant height dI/dV maps from Fig. 5(a) were taken. Horizontal black dashed lines [and gray dashed lines in (c)] indicate the energies at which these maps were measured. (b) dI/dV(x,V) map resulting from the spectroscopic line. (c) 1D FFT of the dI/dV map in (b). (d) Calculated band structure of a freestanding 14 ML Pb film. The image presents a part of the full band structure which is similar to the electronic structure of the island in (a)–(c). Arrows indicate different scattering processes responsible for the spectroscopic features observed in (b) and (c). Dashed lines indicate energies at which the constant energy cuts from Fig. 5(c) were calculated. The energy is measured in eV. Note the difference of the energy scales in (a) and (d).
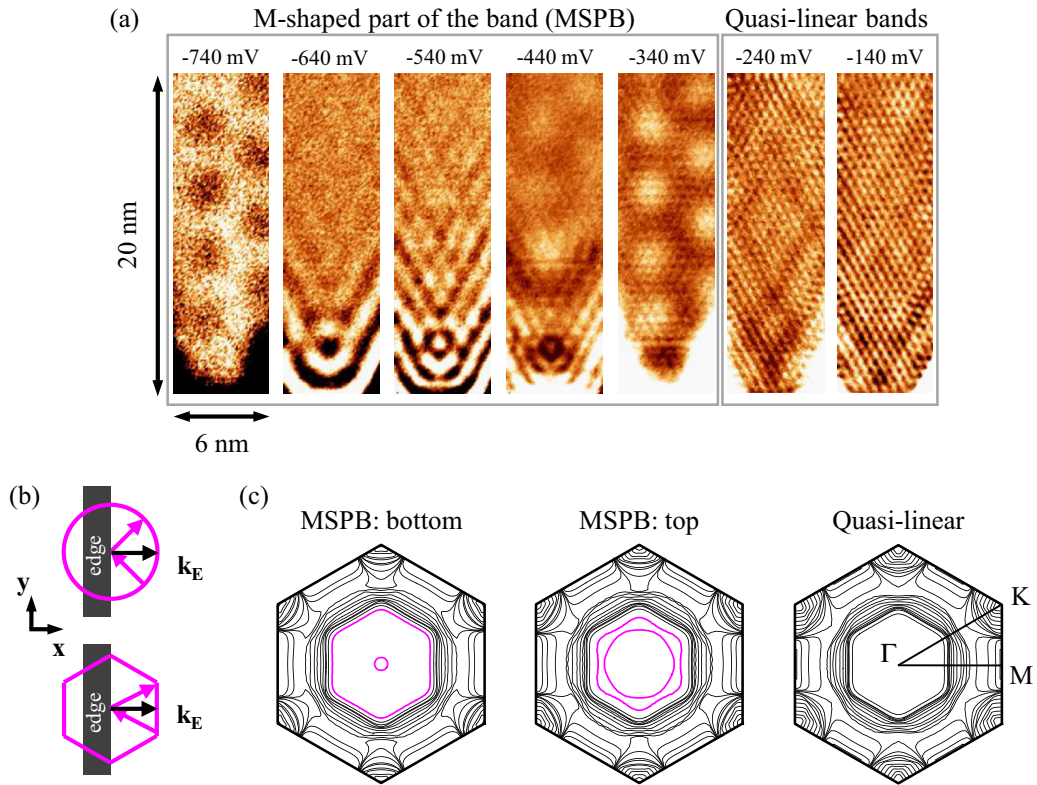
FIG. 5. (a) Constant height dI/dV maps taken on the corner [see the inset of Fig. 4(a)] of the triangular 15-ML island from Figs. 1(b) and 4. The corresponding energies are indicated with the horizontal dashed lines in Figs. 4(a) and 4(c). (b) Schematic drawings illustrating the construction of the wave vector k of the LDOS modulation for two different shapes of the constant energy contours. (c) Calculated constant energy contours of a freestanding 14-ML Pb film. The energies are (from the left to right): −0.23 eV, 0.035 eV, 0.35 eV, and are indicated with dashed lines in Fig. 4(d).

1D fast Fourier transform (FFT) of this image is shown in Fig. 4(c). It can be directly compared with the band structure of the Pb film [93,94], which is shown in Fig. 4(d) along the ΓM direction (direction perpendicular to the islands edge) in a comparable energy range. The arrows of different colors in Fig. 4(d) indicate different scattering channels that give rise to the QPI patterns. The corresponding wave vectors of the QPI patterns are indicated in Fig. 4(c) with the dots of the same color. Note that the QPI pattern wave vector is two times larger than the wave vector of the quasiparticle in the corresponding scattering channel [93,94]. Colored dashed lines in Fig. 4(b) help to link different scattering channels with the observed oscillations in LDOS. The agreement between measured QPI pattern wavelengths and calculated band dispersion is very good. The QPI pattern originating from quasilinear bands between MSPBs have a less sharp signal in the FFT map. Presumably, this is related to the number ($\approx$10) of scattering channels with slightly different QPI pattern wavelengths [see Fig. 4(d)]. Nevertheless, the resulting LDOS modulation still shows a dominant wave vector approximately corresponding to the average wave vector of the group of the quasilinear bands at a given energy. We also note that the intensity of these QPI patterns is strongly reduced on the thick (20–30 ML) islands as the one shown in Fig. 3, where the number of QWS and hence the number of quasilinear bands increases [2].

There is a remarkable difference in the decay length of the QPI patterns originating from the states inside MSPB and

from the states belonging to the quasilinear bands of the QWS between the MSPBs. Consider, for example, the QPI pattern originating from the scattering of the states with parabolic dispersion at the bottom of the MSPB [red arrow in Fig. 4(d)]. They completely vanish at the distance of about 6–7 nm from the edge [red dashed line in Fig. 4(b)]. At the same time, the QPI pattern originating from the scattering between quasilinear bands between MSPBs [green dashed line and green arrow in Figs. 4(b) and 4(d)] do not show any significant decay even in the center of the island, 15 nm away from the edges. This effect is further illustrated in Fig. 5(a), where we show the results of the spatially-resolved dI/dV measurements in the corner of the same 15-ML island (see the black rectangle in the inset of Fig. 4(a)) taken in the Z_{const} mode. The dI/dV maps taken at biases −740 mV and −340 mV (the energies of the bottom and of the top of the MSPB) show a long-range modulation, with the period of approximately 4 nm, due to the effect of the moiré pattern already discussed above. Other short-range modulations are QPI patterns.

The amplitude of the LDOS modulation due to the QPI at a perfect linear defect in a 2D electron gas depends on the distance from the defect as (adapted from Refs. [95,96]):

$$\rho(E, x) \propto e^{-x/L_\phi} \frac{\cos(2k_E x)}{x^\alpha}.$$

The cosine function in this expression reflects the fringes of LDOS of spatial period π/k_E parallel to the step edge due

to QPI [see Fig. 5(b) for the definition of the k_E vector]. The exponential prefactor describes the decoherence of the quasiparticles [95]. The energy-dependent coherence length L_ϕ is related to the coherence lifetime τ ($\tau \propto 1/\Gamma_{lifetime}$) and group velocity v_g through $L_\phi = v_g \tau$. While the coherence lifetime doesn't change much in the energy range we consider [Fig. 2(c)], the group velocity of the quasiparticles is almost one order of magnitude larger inside the quasilinear bands than inside the MSPB. A quantitative analysis shows that the maximum coherence length for the quasiparticles in the MSPB of Fig. 4 is about 4 nm, whereas in the quasilinear bands it is about 30 nm.

Another factor that influences the spatial decay length of the QPI patterns is the anisotropy of the band structure, more precisely, the shape of the constant energy contours of the bands, which is reflected in the denominator exponent α [93,96,97]. For the nearly free electron gas with a circular constant energy contour [see Fig. 5(b), top] $\alpha = 1/2$. Any flat part of the contour parallel to the edge [see Fig. 5(b) bottom] will lead to $\alpha = 0$ and nondecaying QPI pattern in the direction perpendicular to it [96,98]. In Fig. 5(c), we present three computed constant energy contours of the 14 ML Pb film band structure [see also the 3D view of this band on Fig. 1(d)]. The two first constant energy contours from the left, corresponding to the cuts at the bottom and at the top of the MSPB, show that the band dispersion in the central part of the Brillouin zone remains free-electron-like (circular constant energy contour) almost in the whole energy range of the MSPB. At the same time, the constant energy contours are almost perfectly hexagonal outside the MSPB (i.e., for the quasilinear bands), with one side of the hexagon parallel to the edge of the island. We thus expect a faster attenuation of the QPI pattern within the MSPB also from the anisotropy of the band structure.

Both factors (phase coherence length and band anisotropy) thus contribute to the observed difference of the decay lengths of the QPI patterns originating from states within or outside the MSPB.

IV. SUMMARY AND DISCUSSION

Summarizing our results, we provide in this paper a complete analysis of the electronic structure of Pb islands grown on graphene, including a refined study of the QWS complemented by the analysis of the QPI patterns which show up at the surface of the islands.

We conclude that lead films grown on the surface of graphene can be considered as freestanding from the point of view of their electronic structure, at least for energies $|E - E_F| < 1$–1.5 eV. This fact can be attributed to the chemical inertness and large partial band gap of graphene. Same conclusions were deduced from ARPES studies of Pb/graphitic layer [49] and Pb/HOPG [50] band structures. Accordingly, the graphene remains almost unperturbed close to the lead islands, again suggesting a small Pb-graphene coupling.

It is known that a good interface transparency is required for opening a robust superconducting gap in a 2D metal in contact with a 3D superconductor [55,61,62,99–104]. The weak Pb-graphene electronic coupling is thus a priori not favorable for the introduction of superconductivity in graphene below lead islands by proximity effect. To give a more quantitative estimate of the possibly induced superconducting gap, we make use of theoretical results [61–64] derived for the case of a continuous normal metal film separated by a tunneling barrier from a superconductor occupying the half-space below the film. The superconducting gap induced in a normal 2D film depends on the tunneling rate across the metal/superconductor interface, which can be related to the resistance of the interface R_I through [101]:

$$\Gamma_{tunnel} = \frac{\hbar}{2\pi e^2 \nu_{2D} A R_I},$$

where ν_{2D} is the 2D metal DOS at E_F, A is the area of the metal/superconductor contact. In the case of graphene,

$$\nu_{2D} = \frac{2|E_F - E_D|}{\pi \hbar^2 v_F^2},$$

with v_F being the graphene Fermi velocity and E_D the energy of the Dirac point. Since our experimental results [inset of Fig. 2(a)] are in semiquantitative agreement with the results of the dynamical Coulomb blockade measurements of Ref. [60], we utilize the mean value of the product $AR_I = 3.7 \ 10^{-12} \ \Omega \cdot m^2$ from the latter reference. The doping level of the surface graphene layer in our sample is estimated [67] (from the measurements of the intervalley QPI pattern on graphene [68,69] and from the position of the Van Hove singularities [70,71]) to be $n < 3.5 \times 10^{11} \ cm^{-2}$ ($E_F - E_D < 75$ meV). From this, we estimate the minimal tunneling rate $\Gamma_{tunnel \ min} = 2$ meV $\approx 1.5\Delta_{Pb}$ (bulk lead $\Delta_{Pb} = 1.35$ meV [105], critical superconducting temperature 7.19 K [11]). According to Ref. [62], the proximity induced gap in graphene DOS below an island should thus be $\Delta_{graphene} > 0.65\Delta_{Pb} \approx 0.9$ meV. This agrees with the conclusion of other studies [61,63], according to which the proximity-induced gap is still a sizable fraction of the bulk superconductor gap even for metal/superconductor junctions of moderate transparency. Such a proximity-induced superconducting gap should be, in principal, detectable on graphene in the vicinity of large Pb islands, owing to the weak backscattering of graphene electrons at the Pb edges. Such measurements should be achievable with the state of the art STM operating at low or ultralow temperature, but in the present work, the sample temperature was too high to address this question.

[1] M. Jałochowski, E. Bauer, H. Knoppe, and G. Lilienkamp, Phys. Rev. B **45**, 13607 (1992).

[2] N. Miyata, K. Horikoshi, T. Hirahara, S. Hasegawa, C. M. Wei, and I. Matsuda, Phys. Rev. B **78**, 245405 (2008).

[3] M. Jałochowski, M. Hoffmann, and E. Bauer, Phys. Rev. Lett. **76**, 4227 (1996).

[4] I. Vilfan, M. Henzler, O. Pfennigstorf, and H. Pfnür, Phys. Rev. B **66**, 241306 (2002).

[5] Y. Qi, X. Ma, P. Jiang, S. Ji, Y. Fu, J.-F. Jia, Q.-K. Xue, and S. Zhang, Appl. Phys. Lett. **90**, 013109 (2007).

[6] R.-Y. Liu, A. Huang, C.-C. Huang, C.-Y. Lee, C.-H. Lin, C.-M. Cheng, K.-D. Tsuei, H.-T. Jeng, I. Matsuda, and S.-J. Tang, Phys. Rev. B **92**, 115415 (2015).

[7] C. M. Wei and M. Y. Chou, Phys. Rev. B **66**, 233408 (2002).

[8] R. Otero, A. L. Vázquez de Parga, and R. Miranda, Phys. Rev. B **66**, 115401 (2002).

[9] M. H. Upton, C. M. Wei, M. Y. Chou, T. Miller, and T.-C. Chiang, Phys. Rev. Lett. **93**, 026802 (2004).

[10] F. Calleja, M. C. G. Passeggi, Jr., J. J. Hinarejos, A. L. Vázquez de Parga, and R. Miranda, Phys. Rev. Lett. **97**, 186104 (2006).

[11] N. Ashcroft and N. Mermin, *Solid State Physics* (Saunders College, Philadelphia, 1976).

[12] Y. Guo, Y.-F. Zhang, X.-Y. Bao, T.-Z. Han, Z. Tang, L.-X. Zhang, W.-G. Zhu, E. Wang, Q. Niu, Z. Qiu *et al.*, Science **306**, 1915 (2004).

[13] Y.-F. Zhang, J.-F. Jia, T.-Z. Han, Z. Tang, Q.-T. Shen, Y. Guo, Z. Q. Qiu, and Q.-K. Xue, Phys. Rev. Lett. **95**, 096802 (2005).

[14] M. M. Özer, J. R. Thompson, and H. H. Weitering, Nat. Phys. **2**, 173 (2006).

[15] D. Eom, S. Qin, M.-Y. Chou, and C. K. Shih, Phys. Rev. Lett. **96**, 027005 (2006).

[16] C. Brun, I.-Po Hong, F. Patthey, I. Y. Sklyadneva, R. Heid, P. M. Echenique, K. P. Bohnen, E. V. Chulkov, and W.-D. Schneider, Phys. Rev. Lett. **102**, 207002 (2009).

[17] S. Qin, J. Kim, Q. Niu, and C.-K. Shih, Science **324**, 1314 (2009).

[18] T. Zhang, P. Cheng, W.-J. Li, Y.-J. Sun, G. Wang, X.-G. Zhu, K. He, L. Wang, X. Ma, X. Chen *et al.*, Nat. Phys. **6**, 104 (2010).

[19] C. Brun, T. Cren, V. Cherkez, F. Debontridder, S. Pons, D. Fokin, M. Tringides, S. Bozhko, L. Ioffe, B. Altshuler *et al.*, Nat. Phys. **10**, 444 (2014).

[20] M. Schackert, T. Märkl, J. Jandke, M. Hölzer, S. Ostanin, E. K. U. Gross, A. Ernst, and W. Wulfhekel, Phys. Rev. Lett. **114**, 047002 (2015).

[21] C. Brun, T. Cren, and D. Roditchev, Supercond. Sci. Technol. **30**, 013003 (2016).

[22] T. Nishio, T. An, A. Nomura, K. Miyachi, T. Eguchi, H. Sakata, S. Lin, N. Hayashi, N. Nakai, M. Machida, and Y. Hasegawa, Phys. Rev. Lett. **101**, 167001 (2008).

[23] T. Cren, D. Fokin, F. Debontridder, V. Dubost, and D. Roditchev, Phys. Rev. Lett. **102**, 127005 (2009).

[24] T. Cren, L. Serrier-Garcia, F. Debontridder, and D. Roditchev, Phys. Rev. Lett. **107**, 097202 (2011).

[25] J. Kim, V. Chua, G. A. Fiete, H. Nam, A. H. MacDonald, and C.-K. Shih, Nat. Phys. **8**, 464 (2012).

[26] L. Serrier-Garcia, J. C. Cuevas, T. Cren, C. Brun, V. Cherkez, F. Debontridder, D. Fokin, F. S. Bergeret, and D. Roditchev, Phys. Rev. Lett. **110**, 157003 (2013).

[27] V. Cherkez, J. C. Cuevas, C. Brun, T. Cren, G. Ménard, F. Debontridder, V. S. Stolyarov, and D. Roditchev, Phys. Rev. X **4**, 011033 (2014).

[28] D. Roditchev, C. Brun, L. Serrier-Garcia, J. C. Cuevas, V. H. L. Bessa, M. V. Milošević, F. Debontridder, V. Stolyarov, and T. Cren, Nat. Phys. **11**, 332 (2015).

[29] T. Zhang, S. Vlaic, S. Pons, A. Assouline, A. Zimmers, D. Roditchev, H. Aubin, G. Allan, C. Delerue, C. David, G. Rodary, and J.-C. Girard, Phys. Rev. B **97**, 214514 (2018).

[30] S. Vlaic, S. Pons, T. Zhang, A. Assouline, A. Zimmers, C. David, G. Rodary, J.-C. Girard, D. Roditchev, and H. Aubin, Nat. Commun. **8**, 14549 (2017).

[31] T.-C. Chiang, Surf. Sci. Rep. **39**, 181 (2000).

[32] P. Echenique and J. Pendry, J. Phys. C: Solid State Phys. **11**, 2065 (1978).

[33] N. V. Smith, Phys. Rev. B **32**, 3549 (1985).

[34] S.-J. Tang, L. Basile, T. Miller, and T.-C. Chiang, Phys. Rev. Lett. **93**, 216804 (2004).

[35] M. Becker and R. Berndt, Phys. Rev. B **81**, 205438 (2010).

[36] N. Speer, S.-J. Tang, T. Miller, and T.-C. Chiang, Science **314**, 804 (2006).

[37] S.-J. Tang, T. Miller, and T.-C. Chiang, Phys. Rev. Lett. **96**, 036802 (2006).

[38] S.-J. Tang, Y.-R. Lee, S.-L. Chang, T. Miller, and T.-C. Chiang, Phys. Rev. Lett. **96**, 216803 (2006).

[39] P. Moras, L. Ferrari, C. Spezzani, S. Gardonio, M. Ležaić, P. Mavropoulos, S. Blügel, and C. Carbone, Phys. Rev. Lett. **97**, 206802 (2006).

[40] T. C. Chiang, AAPPS Bull. **18**, 2 (2008).

[41] P. Moras, D. Topwal, P. M. Sheverdyaeva, L. Ferrari, J. Fujii, G. Bihlmayer, S. Blügel, and C. Carbone, Phys. Rev. B **80**, 205418 (2009).

[42] M. H. Upton, T. Miller, and T.-C. Chiang, Phys. Rev. B **71**, 033403 (2005).

[43] J. H. Dil, J. W. Kim, T. Kampen, K. Horn, and A. R. H. F. Ettema, Phys. Rev. B **73**, 161308 (2006).

[44] W. B. Su, S. H. Chang, W. B. Jian, C. S. Chang, L. J. Chen, and T. T. Tsong, Phys. Rev. Lett. **86**, 5116 (2001).

[45] K. Wang, X. Zhang, M. M. T. Loy, T.-C. Chiang, and X. Xiao, Phys. Rev. Lett. **102**, 076801 (2009).

[46] I.-Po Hong, C. Brun, F. Patthey, I. Y. Sklyadneva, X. Zubizarreta, R. Heid, V. M. Silkin, P. M. Echenique, K. P. Bohnen, E. V. Chulkov, and W.-D. Schneider, Phys. Rev. B **80**, 081409 (2009).

[47] F. Patthey and W.-D. Schneider, Phys. Rev. B **50**, 17560 (1994).

[48] M. Breitholtz, T. Kihlgren, S.-A. Lindgren, H. Olin, E. Wahlström, and L. Walldén, Phys. Rev. B **64**, 073301 (2001).

[49] J. H. Dil, T. U. Kampen, B. Hülsen, T. Seyller, and K. Horn, Phys. Rev. B **75**, 161401 (2007).

[50] Y. Liu, J. J. Paggel, M. H. Upton, T. Miller, and T.-C. Chiang, Phys. Rev. B **78**, 235437 (2008).

[51] Y. Wang, M. Chen, Z. Li, L. Wang, K. He, Q.-K. Xue, and X. Ma, Appl. Phys. Lett. **103**, 242603 (2013).

[52] C. W. J. Beenakker, Rev. Mod. Phys. **80**, 1337 (2008).

[53] A. Allain, Z. Han, and V. Bouchiat, Nat. Mater. **11**, 590 (2012).

[54] Z. Han, A. Allain, H. Arjmandi-Tash, K. Tikhonov, M. Feigel'Man, B. Sacépé, and V. Bouchiat, Nat. Phys. **10**, 380 (2014).

[55] V. E. Calado, S. Goswami, G. Nanda, M. Diez, A. R. Akhmerov, K. Watanabe, T. Taniguchi, T. M. Klapwijk, and L. M. Vandersypen, Nat. Nanotechnol. **10**, 761 (2015).

[56] M. B. Shalom, M. Zhu, V. Fal'ko, A. Mishchenko, A. Kretinin, K. Novoselov, C. Woods, K. Watanabe, T. Taniguchi, A. Geim *et al.*, Nat. Phys. **12**, 318 (2016).

[57] D. Efetov, L. Wang, C. Handschin, K. Efetov, J. Shuang, R. Cava, T. Taniguchi, K. Watanabe, J. Hone, C. Dean *et al.*, Nat. Phys. **12**, 328 (2016).

[58] C. Tonnoir, A. Kimouche, J. Coraux, L. Magaud, B. Delsol, B. Gilles, and C. Chapelier, Phys. Rev. Lett. **111**, 246805 (2013).

[59] F. D. Natterer, J. Ha, H. Baek, D. Zhang, W. G. Cullen, N. B. Zhitenev, Y. Kuk, and J. A. Stroscio, Phys. Rev. B **93**, 045406 (2016).

[60] C. Brun, K. H. Müller, I.-Po Hong, F. Patthey, C. Flindt, and W.-D. Schneider, Phys. Rev. Lett. **108**, 126802 (2012).

[61] A. Volkov, P. Magnée, B. Van Wees, and T. Klapwijk, Phys. C **242**, 261 (1995).

[62] N. B. Kopnin and A. S. Melnikov, Phys. Rev. B **84**, 064524 (2011).

[63] Y. Takane and R. Ando, J. Phys. Soc. Jpn. **83**, 014706 (2013).

[64] C. R. Reeg and D. L. Maslov, Phys. Rev. B **94**, 020501 (2016).

[65] J. Hass, F. Varchon, J. E. Millán-Otoya, M. Sprinkle, N. Sharma, W. A. de Heer, C. Berger, P. N. First, L. Magaud, and E. H. Conrad, Phys. Rev. Lett. **100**, 125504 (2008).

[66] T. Le Quang, Low-Temperature Scanning Tunneling Spectroscopy of Epitaxial Graphene Grown on SiC, Ph.D. thesis, Université Grenoble Alpes (2016).

[67] See Supplemental Material at http://link.aps.org/supplemental/10.1103/PhysRevB.98.195441 for the data taken on graphene at the interface with Pb islands.

[68] P. Mallet, I. Brihuega, S. Bose, M. M. Ugeda, J. M. Gómez-Rodríguez, K. Kern, and J.-Y. Veuillen, Phys. Rev. B **86**, 045444 (2012).

[69] P. Mallet, I. Brihuega, V. Cherkez, J. M. Gómez-Rodríguez, and J.-Y. Veuillen, C. R. Phys. **17**, 294 (2016).

[70] V. Cherkez, G. Trambly de Laissardière, P. Mallet, and J.-Y. Veuillen, Phys. Rev. B **91**, 155428 (2015).

[71] I. Brihuega, P. Mallet, H. González-Herrero, G. Trambly de Laissardiére, M. M. Ugeda, L. Magaud, J. M. Gómez-Rodríguez, F. Ynduráin, and J.-Y. Veuillen, Phys. Rev. Lett. **109**, 196802 (2012).

[72] M. Jałochowski, K. Palotás, and M. Krawiec, Phys. Rev. B **93**, 035437 (2016).

[73] H. P. Klug, J. Am. Chem. Soc. **68**, 1493 (1946).

[74] I. Horcas, R. Fernández, J. Gomez-Rodriguez, J. Colchero, J. Gómez-Herrero, and A. Baro, Rev. Sci. Instrum. **78**, 013705 (2007).

[75] G. Kresse and J. Hafner, Phys. Rev. B **47**, 558 (1993).

[76] G. Kresse and D. Joubert, Phys. Rev. B **59**, 1758 (1999).

[77] J. P. Perdew, K. Burke, and M. Ernzerhof, Phys. Rev. Lett. **77**, 3865 (1996).

[78] H. P. Bonzel, D. Yu, and M. Scheffler, Appl. Phys. A **87**, 391 (2007).

[79] L. Liu, W. Xiao, K. Yang, L. Zhang, Y. Jiang, X. Fei, S. Du, and H.-J. Gao, J. Phys. Chem. C **117**, 22652 (2013).

[80] X. Liu, T. Hu, Y. Miao, D. Ma, P. K. Chu, F. Ma, and K. Xu, J. Appl. Phys. **117**, 065304 (2015).

[81] A. Mahmood, P. Mallet, and J.-Y. Veuillen, Nanotechnology **23**, 055706 (2012).

[82] H. González-Herrero, J. M. Gómez-Rodríguez, P. Mallet, M. Moaied, J. J. Palacios, C. Salgado, M. M. Ugeda, J.-Y. Veuillen, F. Yndurain, and I. Brihuega, Science **352**, 437 (2016).

[83] P. Mallet, F. Varchon, C. Naud, L. Magaud, C. Berger, and J.-Y. Veuillen, Phys. Rev. B **76**, 041403(R) (2007).

[84] M. Müller, N. Néel, S. Crampin, and J. Kröger, Phys. Rev. Lett. **117**, 136803 (2016).

[85] M. Müller, N. Néel, S. Crampin, and J. Kröger, Phys. Rev. B **96**, 205426 (2017).

[86] J. Tersoff and D. R. Hamann, Phys. Rev. B **31**, 805 (1985).

[87] I. B. Altfeder, K. A. Matveev, and D. M. Chen, Phys. Rev. Lett. **78**, 2815 (1997).

[88] B. Slomski, F. Meier, J. Osterwalder, and J. H. Dil, Phys. Rev. B **83**, 035409 (2011).

[89] J. J. Quinn and R. A. Ferrell, Phys. Rev. **112**, 812 (1958).

[90] M. Hupalo, V. Yeh, T. L. Chan, C. Z. Wang, K. M. Ho, and M. C. Tringides, Phys. Rev. B **71**, 193408 (2005).

[91] I. B. Altfeder, V. Narayanamurti, and D. M. Chen, Phys. Rev. Lett. **88**, 206801 (2002).

[92] W. B. Jian, W. B. Su, C. S. Chang, and T. T. Tsong, Phys. Rev. Lett. **90**, 196603 (2003).

[93] L. Petersen, P. Hofmann, E. Plummer, and F. Besenbacher, J. Electron Spectrosc. Relat. Phenom. **109**, 97 (2000).

[94] K. Schouteden, P. Lievens, and C. Van Haesendonck, Phys. Rev. B **79**, 195409 (2009).

[95] J. Kröger, L. Limot, H. Jensen, R. Berndt, S. Crampin, and E. Pehlke, Prog. Surf. Sci. **80**, 26 (2005).

[96] S. Lounis, P. Zahn, A. Weismann, M. Wenderoth, R. G. Ulbrich, I. Mertig, P. H. Dederichs, and S. Blügel, Phys. Rev. B **83**, 035427 (2011).

[97] P. Avouris, I.-W. Lyo, R. Walkup, and Y. Hasegawa, J. Vac. Sci. Technol. B: Microelectron. Nanometer Struct. Process. Meas. Phenom. **12**, 1447 (1994).

[98] M. Bouhassoune, B. Zimmermann, P. Mavropoulos, D. Wortmann, P. H. Dederichs, S. Blügel, and S. Lounis, Nat. Commun. **5**, 5558 (2014).

[99] G. Fagas, G. Tkachov, A. Pfund, and K. Richter, Phys. Rev. B **71**, 224510 (2005).

[100] C. Ojeda-Aristizabal, M. Ferrier, S. Guéron, and H. Bouchiat, Phys. Rev. B **79**, 165436 (2009).

[101] N. B. Kopnin, A. S. Mel'nikov, I. A. Sadovskyy, and V. M. Vinokur, Phys. Rev. B **89**, 081402 (2014).

[102] I. Borzenets, Y. Shimazaki, G. Jones, M. F. Craciun, S. Russo, M. Yamamoto, and S. Tarucha, Sci. Rep. **6**, 23051 (2016).

[103] J. C. Cuevas, D. Roditchev, T. Cren, and C. Brun, in *The Oxford Handbook of Small Superconductors*, edited by A. V. Narlikar (Oxford University Press, Oxford, 2017), Chap. 4, pp. 108–144.

[104] L. Bretheau, I. Joel, J. Wang, R. Pisoni, K. Watanabe, T. Taniguchi, and P. Jarillo-Herrero, Nat. Phys. **13**, 756 (2017).

[105] M. Ruby, B. W. Heinrich, J. I. Pascual, and K. J. Franke, Phys. Rev. Lett. **114**, 157001 (2015).